Received: 28 October 2022 | Revised: 19 September 2023 | Accepted: 29 September 2023

DOI: 10.1002/dep2.258

The Depositional Record Open Access
A journal of the International Association of Sedimentologists
WILEY

ORIGINAL RESEARCH ARTICLE

Biogenicity of amorphous organic matter and bacteriomorph acritarchs preserved in wrinkle structures from the Ediacaran Cíjara Formation, Spain

J. Javier Álvaro[1] | **José E. Ortiz**[2] | **Carlos Neto de Carvalho**[3] | **Ignacio López-Cilla**[2] | **Yolanda Sánchez-Palencia**[2] | **Trinidad Torres**[2]

[1]Instituto de Geociencias (CSIC-UCM), Madrid, Spain

[2]Laboratorio de Estratigrafía Biomolecular, E.T.S.I. Minas y Energía de Madrid, Universidad Politécnica de Madrid, Madrid, Spain

[3]Naturtejo UNESCO Global Geopark, Geology Office of the Municipality of Idanha-a-Nova, Idanha a Nova and Instituto D. Luiz, University of Lisbon, Lisbon, Portugal

Correspondence
J. Javier Álvaro, Instituto de Geociencias (CSIC-UCM), Dr. Severo Ochoa 7, Madrid 28040, Spain.
Email: jj.alvaro@csic.es

Funding information
Ministry of Science and Innovation, Spain, Grant/Award Number: Spanish Project PID2021-125585NB-I00

Abstract

Establishing the biogenicity of sedimentary surface textures with unresolved microbial origin is critical to any environmental and geobiological interpretation of clastic settings. Here, some Ediacaran wrinkle structures and associated carbonaceous greywacke samples containing mat fragments rich in 'bacteriomorph acritarchs' are investigated. Their biogenicity was evaluated with transmitted light and scanning electron microscopy, epifluorescence and Raman spectroscopy, and confirmed by the presence of distinct cyanobacterial biomarkers. The comparison of results yielded by these techniques validates the use of Raman spectroscopy on Neoproterozoic kerogen (organic-walled microfossils and amorphous organic material) under low metamorphic conditions. Raman spectrographs also allowed recognition of associated rare-earth element-rich phosphate (monazite) and subsidiary metal sulphide concentrations, and interpreted as a result of biosorption and/or mat trapping under normal oxic conditions. These microbial mat features represent cyanobacterial bloom-forming *Bavlinella* acritarchs, which characterise eutrophic episodes in a semi-enclosed retroarc basin sandwiched between an active Cadomian arc and West Gondwana.

KEYWORDS

biomarkers, cyanobacteria, Ediacaran, Gondwana, Raman spectra

1 | INTRODUCTION

Investigating organic matter remains in Precambrian rocks is key for improving analytical techniques to search for traces of life, past or present, on other planets. Raman spectroscopy has been selected as one of the first-step analytical instruments for the Mars 2020 and ExoMars 2022 rover missions (Hutchinson et al., 2014; Rull et al., 2017; Vago et al., 2017), and represents the advantages of remote spectroscopic sensing for the detection of biogeochemical spectral signatures. However, the spectral signatures obtained from Archaean and Proterozoic kerogen, with contrasted microbial origin, is similar to spectra obtained from poorly ordered carbonaceous material that arise through abiotic processes: these structures are in a poor state of preservation and

exhibit relatively simple morphologies that have consequently resulted in endless doubts about their biogenicity (Allwood et al., 2006; McCollom & Seewald, 2006; Pasteris & Wopenka, 2003). Post-depositional processes after microbial fossilisation, such as burial, biogeochemical degradation, diagenetic to metamorphic conditions and hydrothermal fluid circulation commonly alter or erase the microfossil original features, challenging the interpretation of morphological diagnostic characters, and the ultrastructure and biogeochemistry of microbial remains. Therefore, there is no agreement as to how to determine by Raman spectroscopy a biogenic signal for Precambrian thermally altered material (Foucher et al., 2015; Schiffbauer et al., 2012).

Microbially induced sedimentary structures (MISS) are primary sedimentary structures formed by the interaction of microbial communities with sediment and physical agents of erosion, deposition and transportation, and can be recognised on bedding planes and within beds (Noffke et al., 2001, 2022). Due to their preservation in the geological record since Archaean times (Noffke et al., 2003, 2006a, 2006b), they are potential candidates for Raman analysis of their kerogen remains (Schieber et al., 2007). In fact, MISS have been listed as targets for the Mars Exploration Rover Program (CASEM, 2007; Noffke, 2021).

However, many MISS share identical or similar morphologies with features generated by non-microbial processes, and so are not diagnostic of biological activity through visual comparison alone (Bayet-Goll & Daraei, 2020; McLoughlin et al., 2008; Menon et al., 2016; Pratt, 2021; Pratt & Ponce, 2019). To solve this dilemma, Noffke (2009, 2021) introduced a series of 'criteria for biogenicity' to distinguish MISS, including their exclusive distribution on a characteristic depositional facies recording clear water, moderate wave energy and quartz sand. Nevertheless, such a restricted biogenic concept has been criticised, among others, by Davies et al. (2016) who proposed the descriptive term 'sedimentary surface textures' for pseudo-MISS with unresolved microbial origin.

The aim of this paper is to study the limits of Raman spectroscopy in the identification of microbial biogeochemical signatures from some Ediacaran (late Neoproterozoic) wrinkle structures, considered as sedimentary surface textures or pseudo-MISS, which subsequently recorded late diagenetic to low-anchizone metamorphic conditions during the Variscan (Mid Devonian to Late Carboniferous) orogeny. To solve possible biogenic uncertainties, the Raman spectroscopic analysis of carbonaceous material was completed with transmitted light microscopy, epifluorescence, scanning electron microscopy (SEM) and biomarker studies.

2 | GEOLOGICAL AND STRATIGRAPHIC BACKGROUND

This study is focussed on some wrinkle structures preserved in the Cíjara Formation, a heterolithic siliciclastic unit, up to 5000 m thick at its stratotype (along the Estenilla river to its outlet into the Cíjara reservoir), composed of conglomerates, sandstones, greywackes, shales and subsidiary breccia interbeds and ubiquitous phosphatic clasts and crusts (Álvaro et al., 2016, 2019). This formation occurs in the Central Iberian Zone of the Iberian Massif (Figure 1A), and represents the terrigenous sedimentation derived by the erosion and denudation of an uplifting orogenic belt fringing the Iberian margin of West Gondwana, known as the Cadomian arc (Álvaro & Lorenzo, 2022; Sánchez García et al., 2019). Due to stepwise processes of emersion, erosion and final collapse, the late Ediacaran sedimentation of the resulting Cadomian retroarc basin was episodically interrupted by episodes of erosion and non-deposition. As a result, the Cíjara Formation is sandwiched between two major unconformities that range from angular discordances to paraconformities: (i) the Lower Alcudian-Domo Extremeño Group/Cíjara Formation contact separating two sedimentary packages with different styles of deformation, which represents the so-called 'late Cadomian Folding event' (Talavera et al., 2015); and (ii) the Cíjara/Pusa formations contact, which is commonly marked by decametre-scale megabreccia beds reflecting the final Cadomian orogenic collapse (Álvaro & Lorenzo, 2022) (Figure 1B). The fossil record of the Cíjara Formation is scarce and restricted to two 'bacteriomorph acritarchs', *Bavlinella faveolata* Shepeleva, 1962 (=*Sphaerocongregus variabilis* Moorman, 1974) and *Palaeogomphosphaeria cauriensis* Palacios Medrano (1989), and two trace fossils, *Gordia marina* and *Helminthoidichnites* isp., pointing to a late Ediacaran age, although its upper part likely belongs to the Fortunian (basal Cambrian; Jensen & Palacios, 2016; Palacios Medrano, 1989; Sequeira, 2011). The formation includes numerous slope-related event deposits characterised by the presence of tool, bounce and flute marks, and common channelised deposits associated with slumps and olistostromes reflecting palaeocurrents towards the northeast (Figure 2A). The abundance of coeval fracturing and fissuring in a substrate submitted to episodic uplift and tilting of blocks is emphasised by the abundance of hydrothermal veining and reworking of their vein quartz clast counterparts (Álvaro et al., 2019).

When the conditions recorded in the retroarc depocentre were tectonically stable, sedimentation mainly recorded the onset of shoaling-upward cycles, up to 12 m thick. Each coarsening-upward cycle displays a vertical succession from structureless greywacke/shale, locally

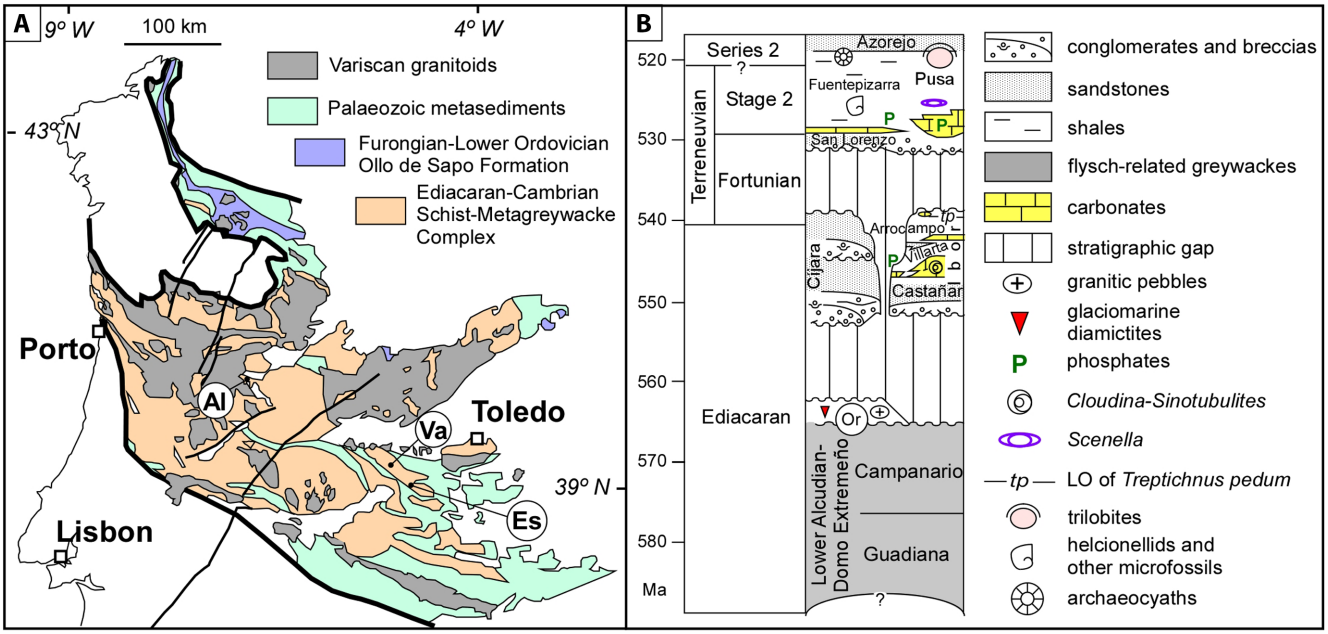

FIGURE 1 Geological and stratigraphic setting of analysed samples. (A) Geological sketch of the Central Iberian Zone; Al, Alagón river bank section; Es, Estenilla river bank section; Va, Valdelacasa Anticline; based on Álvaro and Lorenzo (2022). (B) Stratigraphic chart of the upper Ediacaran–Terreneuvian from the Central Iberian Zone showing the targeted Cíjara Formation; Or, Orellana detrital zircon age (565 ± 4 Ma; Linnemann et al., 2018); based on Álvaro et al. (2019).

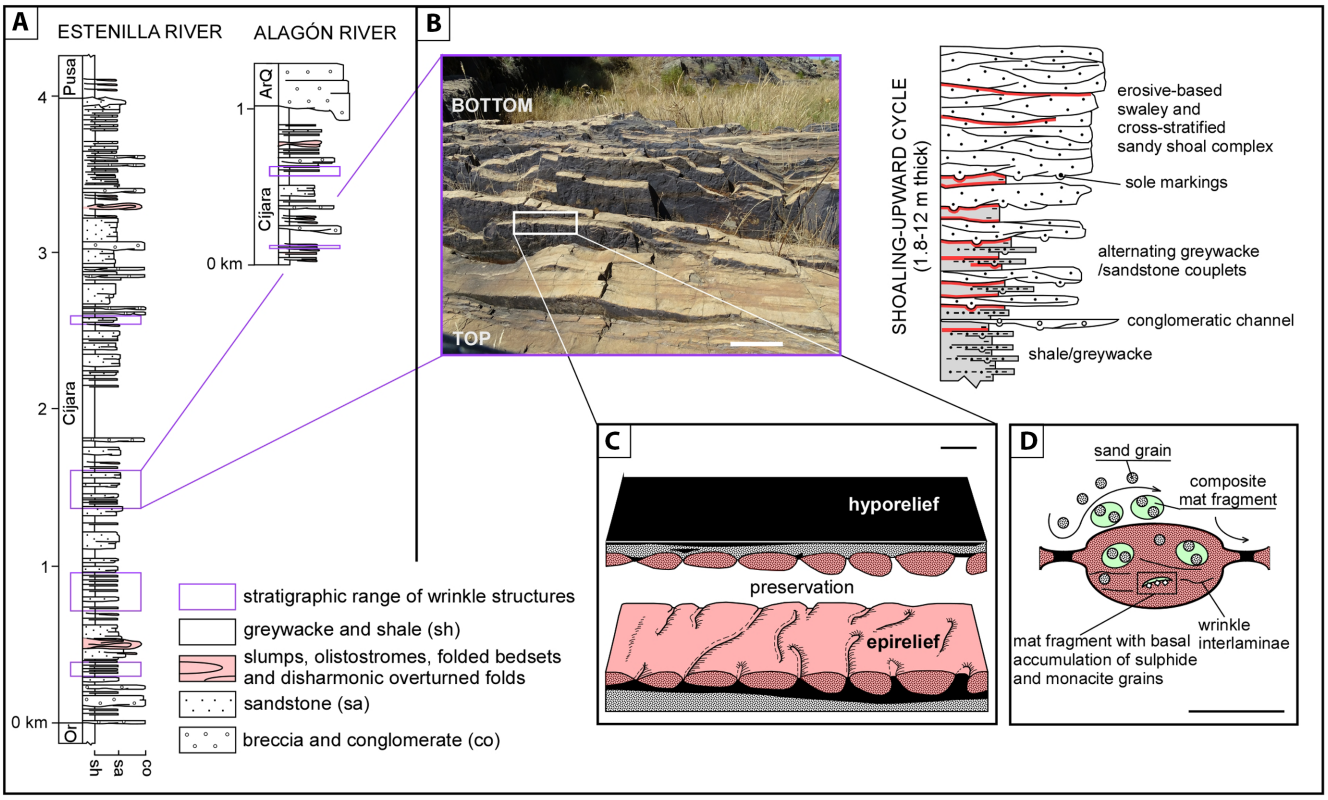

FIGURE 2 Stratigraphic, sequential and intra-wrinkle setting of mat fragments. (A) Stratigraphic logs of the Cíjara Formation from the Estenilla and Alagón river banks, with location of wrinkle structures; ArQ, Armorican Quartzite Formation s.l., Or, Orellana Formation. (B) Field aspect and line drawing of shoaling-upward cycles, up to 12 m thick, with setting of purple to reddened wrinkle structures; scale bar = 5 cm. (C) Preservation of wrinkle structures as hyporeliefs and epireliefs; scale bar = 2–4 mm. (D) Reconstruction of sand grains and composite mat fragments rolling on wrinkle structures, and their preservation within them (modified from Mariotti et al., 2014; Vodrážková et al., 2018); scale bar = 2–4 mm.

interrupted by conglomeratic interbeds, to greywacke/sandstone alternations and amalgamated cross-stratified sandstone beds (Figure 2B). The upward transition from shale to sandstone is gradational, whereas the cycle contacts are abrupt. These trends reflect seaward progradation of nearshore sandy shoal complexes (towards the north-east) during times of rapid sediment influx yielded by the neighbouring orogenic arc (Álvaro et al., 2019). Some shale/greywacke and shale/sandstone contacts are sharp, reddish in colour and exhibit wrinkle structures (Figure 2B,C). Vertical arrangement of some strata, controlled by the Variscan deformation, allows recognition of well-preserved epirelief and hyporelief surfaces, which display wrinkle anastomosing and winding, low-relief, flat-topped ridges bounded by intervening depressions in the millimetre size range (Figures 2C,D and 3A).

3 | SAMPLES AND METHODS

Wrinkle structures of the Ediacaran Cíjara Formation were sampled along the Estenilla and Alagón river banks, in the vicinity of Gamonero and Cachorrilla (Canchus de Ramiro gorge) villages respectively (Figure 1A). They were petrographically characterised using a combination of methods, including transmitted light microscopy and fluorescent imaging, as well as SEM operating in back-scattered electron (BSE) image and energy dispersive X-ray (EDS) analysis at the Museo Nacional de Ciencias Naturales, Madrid. The SEM observations were made on both thin-sections and freshly broken surfaces, after ultrasonic cleaning with alcohol, using a Cambridge Stereoscan 360 and a FEI-Philips ESEM-FEG Quanta 200F. Semiquantitative analyses of submicron-sized spots were performed with an EDAX Genesis 4000 energy dispersive spectrometer on the

FIGURE 3 Field aspect of sedimentary surface structures from the Cíjara Formation. (A) Bedded superposition of patches with reticulate wrinkle structures (arrowed) preserved on the sole of a greywacke bed (level b), embedded between two MISS-free levels (a, c). (B) Lower surface of a greywacke layer, about 5 cm thick, showing wrinkle structures following linear to slightly curved shallow ridges, interrupted by small bulges (black arrows) and microbial sand chips, some of them contorted (white arrows). (C) Wrinkle structures with belts of continuous, broad and flat-topped crests grading into shorter, more irregular and round-topped crests from the top of a greywacke bed. (D) Lower surface of a greywacke layer covered with wrinkle structures following a linear arrangement of shallow ridges. All images from the Estenilla river bank, except F from the Alagón river bank; scale bars = 2 cm (A, B, D) and 1 cm (C).

SEM, and measurements were confirmed on a JEOL JXA-8200 WD/ED Superprobe. Analytical results of BSE and EDS analyses display an error of ±5–7%.

Fluorescent imaging analysis was undertaken to check for the distribution of residual organic matter using fluorescent microscopy at the Instituto de Geociencias, Madrid. Aromatic and certain conjugated organic molecules can cause organically activated luminescence, making residual organic matter the most important activators of fluorescence. Fluorescence was induced by a Hg vapour lamp linked to an imaging microscope equipped with bandpass filter with wavelength from 450 to 490 nm. When containing abundant organic matter, the rock shows strong fluorescence in both green and purple exciting lights. In contrast, the rock exhibits very weak or no fluorescence with little or no organic matter (Mastandrea et al., 2006).

Kerogen extraction was also prepared at the Instituto de Geociencias, through acid maceration. Samples of *ca* 50 g were fragmented (6–10 g) and macerated in 40% hydrofluoric acid over 2 weeks. The resulting residue was boiled in concentrated hydrochloric acid to remove fluorides, and then filtered through 15 and 20 μm mesh membranes. Centrifugation and other aggressive steps were eliminated, and the filtration was done with a vacuum inversion system with filtered water, in which the air inlet (to clear the pores of the filter in vacuum inversion system) is replaced by filtered water, which decreases the violence of the process. Permanent mounts were prepared by mixing precipitate with epoxy resins (the more recent samples in Petropoxy 154) on permanent glass slides. Slides were examined and photographed under transmitted light with a Zeiss Axio Imager M1 microscope equipped with a computerised Axiocam HRc microcamera. The three-dimensional digital reconstruction of acritarchs was achieved with CINEMA 4D Studio R14 software.

The non-intrusive and non-destructive Raman spectroscopy technique (confocal Raman microscopy, Thermo Fisher DXR spectrograph) of the Museo Nacional de Ciencias Naturales was used to characterise carbonaceous material both in thin section and extracted kerogen after acid maceration. The light at 532 nm of a frequency doubled Nd: YVO4 DPSS solid laser (maximum power 30 mW) was used for excitation. Spectral data were analysed with Thermo Scientific OMNIC Series Software. The interference due to high fluorescence caused by the diffuse presence of hydrogen and residual mineral matter was removed by a baseline subtraction procedure, where baseline points at 1000 and 1850 cm^{-1} were fixed for all the spectra. After removal of the background, the deconvolution of the collected Raman spectra was performed by using computational chemistry software Gaussian-16/2017 (Gaussian, Inc., 2017). Voigt functions have been used for the fitting procedure because this function corresponds to the convolution of the phonon mode (Lorentzian profile) with the resolution of the optical setup (Gaussian profile). The choice of a six-band deconvolution was made on the basis of sound foundation, higher accuracy and reproducibility of the fit (see further details in Catelani et al., 2014; Zanatta & Ferri, 2007).

Biomarker analysis of eight wrinkle structures preserved in greywackes and homogeneous shales (free of wrinkle structures) from the Cíjara Formation was performed at the Biomolecular Stratigraphy Laboratory of the E.T.S.I. Minas y Energía in Madrid following the protocol of Ortiz et al. (2010). For each sample, between 3.1 and 5 g of dried samples (50°C, 24 h) was ground, from which biomarkers were extracted with an accelerated solvent extractor (Dionex ASE 200). Free lipids were extracted with dichloromethane (DCM)/MeOH (2:1) at 1500 psi and 175°C. The heating phase was 8 min and the static extraction time 5 min. The extracts were concentrated using a rotary evaporator. Prior to analysis using gas chromatography–mass spectrometry (GC–MS), acidic and polar fractions were methylated with trimethylsilyldiazomethane and silylated with a mixture of N,O-bis(trimethylsilyl)trifluoroacetamide (BSTFA) and pyridine at 70°C for 2 h. Samples were injected into an HP 6890 gas chromatograph equipped with a selective mass detector (HP 5973) and an ATM-5 column (250 × 0.25 mm; 0.20 μm). Prior to analysis, an internal standard (decafluorobiphenyl) with a concentration of 1 μg/L was added to the extracts in order to quantify the compounds. Helium was the carrier gas and the oven temperature was programmed from 60 to 300°C (held 20 min) at 6°C/min and the injector was maintained at 275°C. Components were assigned with the Data Analysis program and the Wiley Library; *n*-alkane distributions were obtained from the *m/z* 57 chromatograms (base peak), the *n*-alkanoic acids from *m/z* 74 and the monosaccharides from *m/z* 204.

Finally, whole-rock major and trace and rare-earth element (REE) compositions were determined at ACME Laboratories, Vancouver, Canada. $LiBO_2$ fusion followed by X-ray fluorescence spectroscopy (XRF) analysis was used to determine major elements. Rare-earth and refractory elements were measured by inductively coupled plasma-mass spectrometry (ICP-MS) following lithium metaborate–tetraborate fusion and nitric acid digestion on a 0.2 g sample. For base metals, a 0.5 g sample was digested in aqua regia at 95°C and analysed by inductively coupled plasma–atomic emission spectrometry (ICP-AES). Analyses of standards and duplicate samples indicate

precision of better than 1% for major oxides and 3 to 10% for minor and trace elements.

4 | RESULTS

Reddened greywacke to very fine-grained sandstone bed surfaces exhibiting wrinkle structures and homogeneous shales of the Cíjara Formation were sampled in two sections, along the Estenilla stratotype (south-east edge of the Valdelacasa Anticline) and Alagón river banks (northern flank of the Penha Garcia-Cañaveral Syncline; Jensen & Palacios, 2016; Figure 1A). Wrinkle structures were analysed at three scales, which include the mesoscale (1–100 mm), the microscale (10–1000 μm) and some individualised 'bacteriomorph acritarchs' and amorphous carbonaceous remains (<10 μm) extracted by acid maceration. Five analytical approaches were envisaged to document the biogenicity of the Cíjara wrinkle structures: petrographic microscopy, epifluorescence, SEM, Raman spectroscopic and biomarker analyses. The REE + Y signatures of the greywacke host rock were analysed to infer redox conditions of the original marine substrate.

4.1 | Wrinkle structures (mesoscale, 1–100 mm)

Several reddish wrinkle structures rich in carbonaceous fragments were selected for analysis. Wrinkle to wavy structures, mainly preserved on upper and lower bedding surfaces, are characterised by corrugated surfaces forming networks of reticulated flat-topped ridges, ranging in height from 1 to 4 mm, separated by flat to slightly depressed areas (Figure 3A through D). Ridges are straight to slightly curved, sinuous to irregular, and rarely bifurcate. Ridges contain, and alternate with, isolated to clustered, carbonaceous fragments and lumps, mainly millimetre-sized but up to 6 cm across in inter-wrinkle laminae, embedded in a greywacke-shale matrix. Mat fragments can be single or composite, formed by smaller lumps, and can be contorted grading into overfolded rolled-up fragments (Figure 3B).

4.2 | Transmitted light microscopy (microscale, 10–1000 μm)

Carbonaceous fragments occur as subangular fragments (Figure 4A), single wisps (Figure 4B,C) and composite fragments including greywacke and silty subunits. They can locally show overfolding and contorted internal textures mimicking the so-called 'rolled-up' mat fragments (Figure 4D). Directly below carbonaceous strings, numerous partly oxidised opaque minerals occur giving the greywacke host-rock a reddish aspect (Figure 4E,F). Scattered opaque spots are largely iron oxyhydroxides. Carbonaceous strings are commonly lined by mica flakes (mainly muscovite) displaying random orientations.

4.3 | Epifluorescence (microscale, 10–1000 μm)

Epifluorescence observations were aimed to assess the distinct interlayering of greywacke/siltstone and organic matter strings (Hackley et al., 2021), in order to select targets for the forthcoming analyses. Under epifluorescence microscopy, some interlaminae and reworked mat clasts, up to 2 mm thick, showed a strong fluorescence under green to blue exciting light. This is contrasted by the absence or weak fluorescence of silty strings and networks of mica flakes.

4.4 | Scanning Electron Microscopy (scale <10 μm)

Once the fluorescent interlaminae with potential carbonaceous material were selected, different energy dispersive spectroscopy analyses confirmed that monazite group phosphates are relatively common lining the lower part of

FIGURE 4 Case-study photomicrographs reflecting the erosion, transport and deformation of microbial mat stabilised substrates, associated with the precipitation of 'anoxic' minerals. (A) Contorted carbonaceous fragment with right frayed edge embedded in an unsorted coarse-grained sandstone. (B) Carbonaceous lumps embedded in a silty matrix. (C) Folded-over carbonaceous wisp. (D) Mixture of carbonaceous lumps (back arrows) and 'rolled-up' mat fragments (white arrows) embedded in a clayey matrix. (E) Wavy laminated pyritic bed in a carbonaceous-rich shale forming an ironstone hardground. (F) Single pyritic striped siltstone. (G) Sub-millimetre couplets of organic matter-rich siltstone (greenish) and poor claystone (darker) interlaminae. (H) Detail of previous sample showing quartz grains (Q) embedded in an homogeneous mass of amorphous organic matter, locally punctuated by carbonaceous fragments (arrowed). (I) Submillimetre-thick MISS with basal asymmetrical domal accumulation of dense sulphide and phosphatic minerals. (J–K) Selection of sulphide and phosphatic minerals underlying carbonaceous organic matter stringers. (L–N) Different EDS spectra of REE-rich phosphate (monazite) minerals. A–F in transmitted light, G,H in epifluorescence, and I–K are BSE-SEM images; scale bars = 500 μm (A–C), 1 mm (D–F), 200 μm (G), 100 μm (H, I), 10 μm (J) and 30 μm (K).

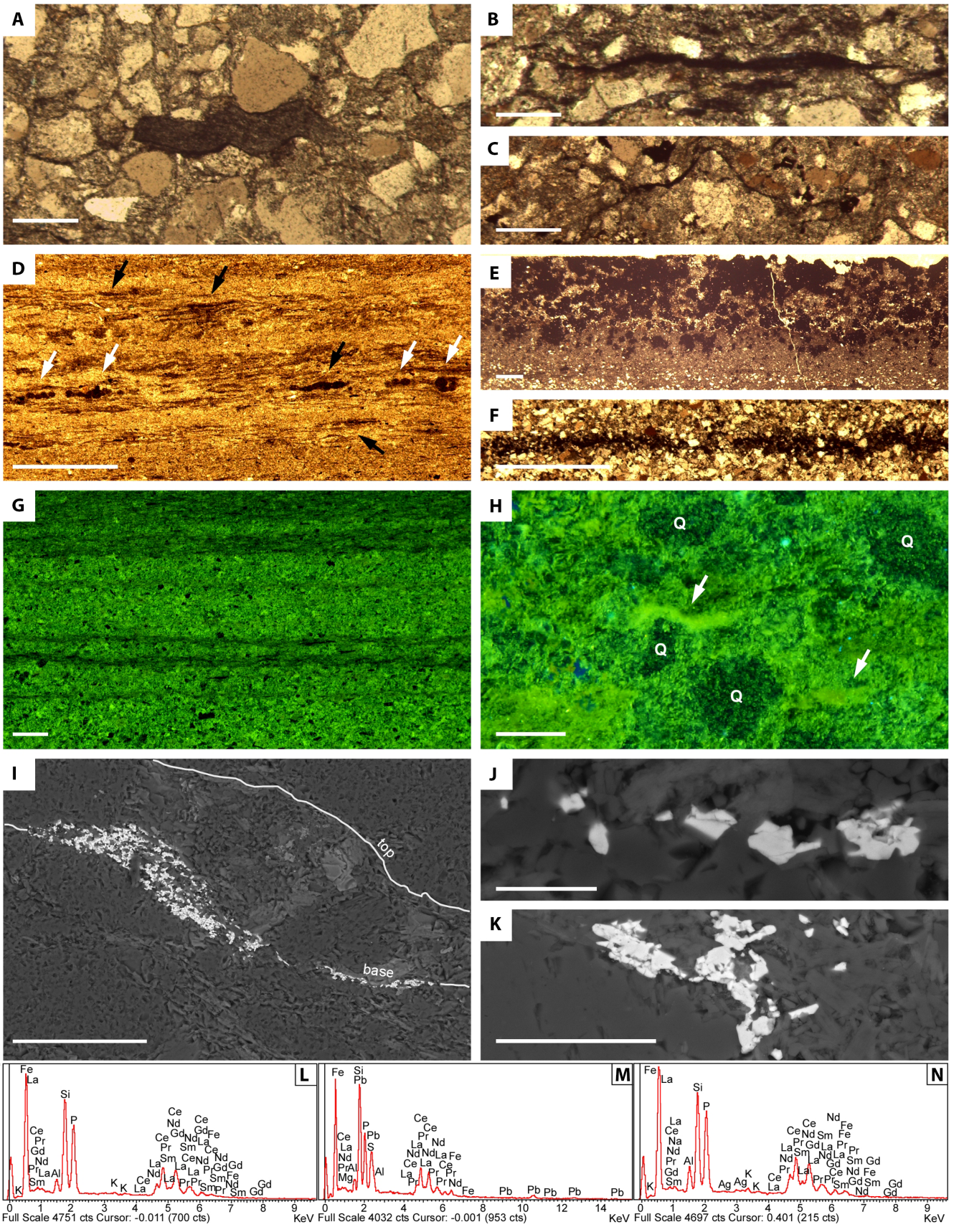

wrinkle interlaminae. The monazite grains contain up to 75% oxides of light REE (Ce > La > Nd > Pr), which occur associated with subsidiary S (<5%) and Pb-Cu-Zn (<5%), reflecting the scattered presence of metal sulphides. Due to the virtual absence of Y, no xenotime can be recognised (Figure 4I, L,M,N).

Other distinct minerals highlighting the basal part of some wrinkle interlaminae form thin, distinct and laterally extensive horizons, up to 1 cm thick, rich in authigenic reducing minerals, such as pyrite, calcite, ferroan dolomite and ankerite (Figure 4J,K). The pyritic content is very variable ranging from carbonaceous laminated clustered with tiny pyrite grains to pyrite laminae arranged in discontinuous wavy textures. Subsequent weathering of these ferroan minerals led to the bedded reddish-stained intervals rich in iron oxyhydroxides that characterise the wrinkle structures (Figure 3A through D).

4.5 | Raman spectroscopy (scale <10 µm)

Laser-spot Raman analysis allowed identification of carbonaceous fragments and associated minerals at a scale <10 µm. The Raman analyses were performed on thin sections of various amorphous organic matter (AOM) remains and acritarch specimens extracted after acid maceration. The Raman spectral signal of kerogen is recorded in a 'first-order' window between 1000 and 2000 cm^{-1} and a 'second-order' one between 2000 and 3500 cm^{-1}. Bands in the latter are generally hidden by fluorescence for low mature samples (Beyssac et al., 2002) and were not observed in this study.

Analysis of AOM displays two distinct bands at *ca* 1350 and 1600 cm^{-1}, although with marked differences in widths and intensities (Figure 5A). In addition, three supplementary bands were yielded by individual acritarchs, at *ca* 1220, 1500 and 1630 cm^{-1} (Figure 5B,C). The Raman spectra of some associated minerals embedded in the targeted AOM contain vibration modes around 1085 to 1100 cm^{-1}, 1435 to 1445 cm^{-1} and 710 to 740 cm^{-1} ranges.

4.6 | Biomarkers (scale <10 µm)

Two targets were selected for biomarker analysis: (i) wrinkle interlaminae marking the base and top of greywackes, and (ii) greenish homogeneous shales that yielded the richest content in acritarchs. Greywacke and shale samples poor in acritarchs, after acid maceration, yielded no significant biomarker peaks. The samples rich in micron-sized acritarchs and/or millimetre-sized mat fragments showed the presence of *n*-alkanes, fatty acids (FAs) and monosaccharides. In general, samples

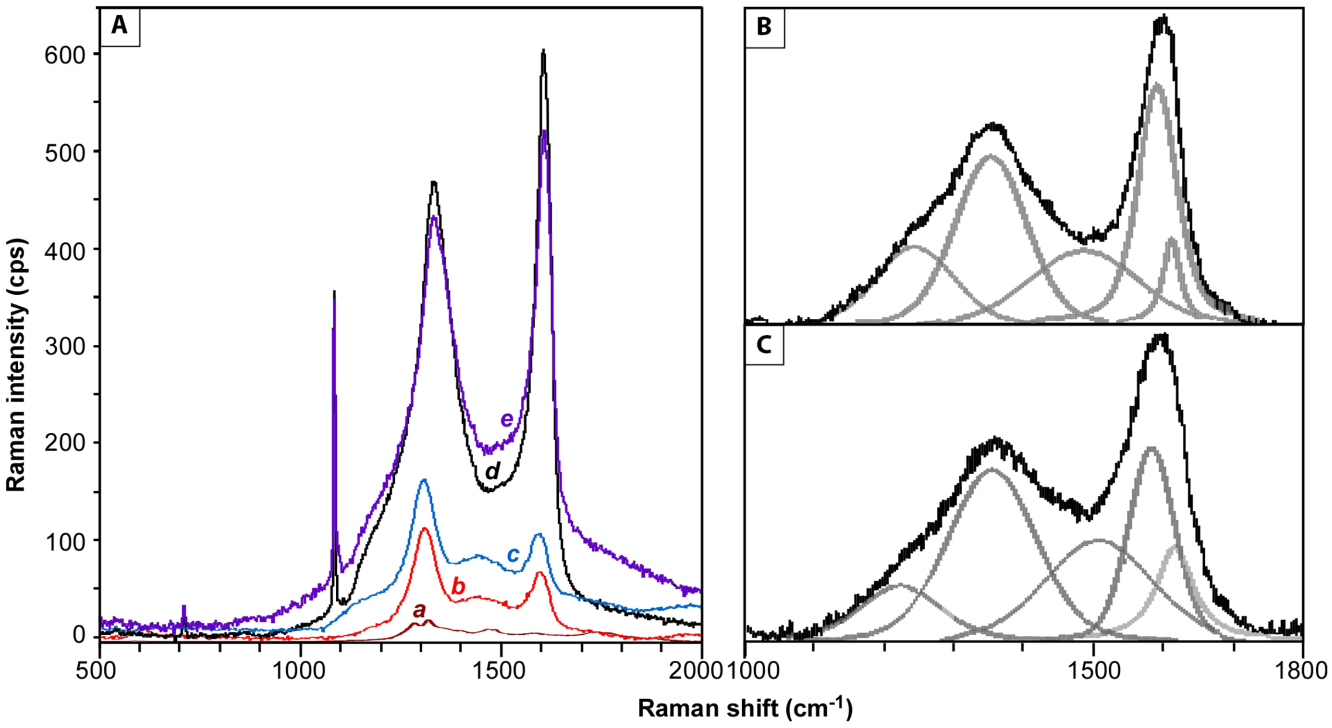

FIGURE 5 Selection of Raman spectra. (A) Spectra of amorphous organic matter remains, without applying deconvolution techniques, at spatial resolution of *ca* 5 µm (labelled *a*) and *ca* 1 µm (*b*–*e*); peak positions at 711, 1085, 1435 and 1580 cm^{-1}. (B, C) Spectra of selected acritarchs (*Bavlinella faveolata* in B), and (*P. caurensis* in C): the grey lines represent deconvolution framework by superposition of the Gaussian lines, performed by Gaussian-03 Software, marked by individual local vibrational modes; peak positions at 1200–1250 cm^{-1} band and 1350, 1500, 1580 and 1620 cm^{-1}.

showed an odd carbon number predominance of *n*-alkanes, with a chain length distribution ranging from C_{17} or C_{21} to C_{33}, maximising at C_{21} or C_{27}. Of note, the alkanes 17:1 and 7-methyl-heptadecane occurred in the samples.

Typical chromatograms of FAs from acritarch-rich samples (Figure 6A,B) show a strong predominance of even numbered saturated FAs, ranging from 14:0 to 30:0 or 32:0, with a marked maximum at 16:0. In addition, branched saturated FAs (*iso*-15:0, *anteiso*-15:0; *iso*-16:0, 14-methyl-16:0, *iso*-17:0, *anteiso*-17:0), monounsaturated FAs (MUFA: 16:1ω7, 18:1ω7) and polyunsaturated FAs (PUFA: 18:2ω6, 18:3ω6) were identified in the samples. The samples also showed abundant

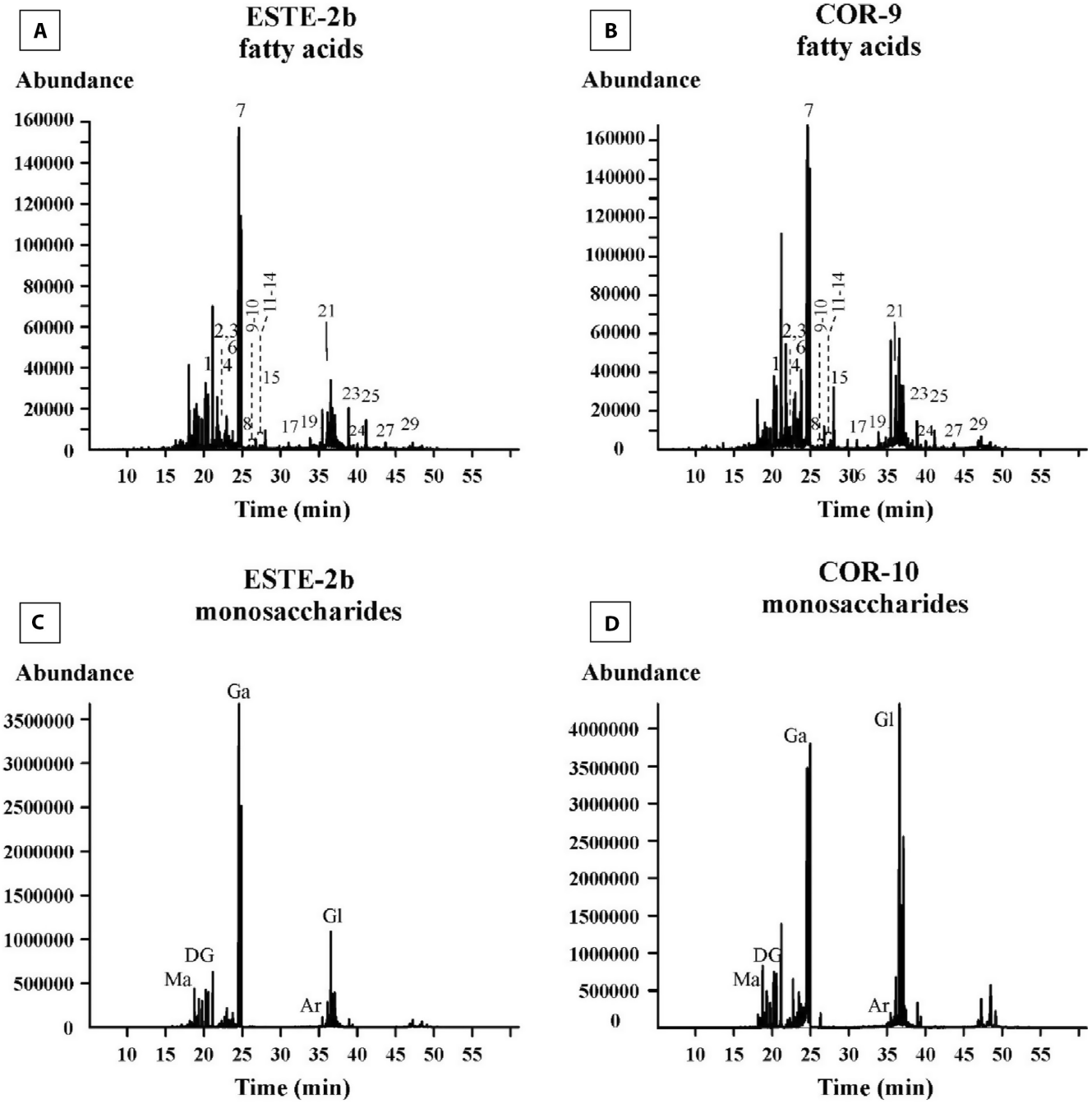

FIGURE 6 Typical chromatograms from selected MISS-bearing greywacke samples: ESTE from Estenilla and COR from Alagón river banks. (A, B) Fatty acids, which maximised at low molecular weight saturated FA (16:0). Peak identification of FA: (1) 14:0; (2) *iso*-15:0; (3) *anteiso*-15:0; (4) 15:0; (5) *iso*-16:0; (6) 16:1; (7) 16:0; (8) 14-methyl 16:0; (9) *iso*-17:0; (10) *anteiso*-17:0; (11) 17:0; (12) 18:2ω6; (13) 18:3ω6; (14) 16:1ω7; (15) 18:0; (16) 19:0; (17) 20:0; (18) 21:0; (19) 22:0; (20) 23:0; (21) 24:0; (22) 25:0; (23) 26:0; (24) 27:0; (25) 28:0; (26) 29:0; (27) 30:0; (28) 31:0; (29) 32:0. (C, D) Monosaccharides. Peak identification of monosaccharides: (Ma) mannose; (Gl) glucose; (Ga) galactose; (Gl) D-glucopyranose; (Ar) arabinose.

monosaccharides, such as mannose, glucose, galactose, allose, D-glucopyranose and arabinose, among others (Figure 6C,D).

4.7 | Geochemical signatures of host rock

The greywacke-rich composition of the Cíjara samples, with and without wrinkle structures, is represented by values ranging from 69.1 to 82 wt% SiO_2, 7.9 to 15.4 wt% Al_2O_3 and 3.9 to 6.8 wt% Fe_2O_3 (Table S1). According to the bulk REE concentrations, the analysed samples are depleted in ΣREE relative to the Post-Archaean Australian Shale standard (PAAS; Pourmand et al., 2012). Samples from wrinkle interlaminae show higher values of ΣREE, ranging from 126 to 188 ppm. The result of plotting the REE content versus the PAAS standard yields a broad flat spectrum. The total content in REE is moderate to high (average REE = 119.8 ppm, ranging between 69.5 and 188.9 ppm). Light rare-earth element (LREE) values are slightly to moderately (e.g. samples COR_1 and COR_8) more fractionated than heavy rare-earth element (HREE) ones, although some flat patterns are also present. The presence versus absence of a distinct positive Eu anomaly in the spider-diagrams allows two groups to be distinguished (Figure 7A,B).

The REE ratios were used to calculate Ce [$Ce/Ce^* = Ce_{(SN)}/(0.5Pr_{(SN)} + 0.5La_{(SN)})$] and Pr [$Pr/Pr^* = Pr_{(SN)}/(0.5Ce_{(SN)} + 0.5Nd_{(SN)})$] values, which are close to unity (Figure 7C). The indicator of Eu anomalies [$Eu/Eu^* Eu_{(SN)}/(0.66Sm_{(SN)} + 0.33Tb_{(SN)})$] ranges from 0.96 to 1.3, and that of Y [$Y/Y^* = (Y_{(SN)}/(Er_{(SN)} + Ho_{(SN)})$] is close to 0.5. Other indicators of palaeoredox conditions (McKay et al., 2007) are Y/Ho (25.4–29.8), ΣREE/Ti (0.03–0.05; Figure 7D), U/Th (0.24–0.35), Ni/Co (2.5–4.5), Cu/Zn (0.05–0.38), (Cu + Mo)/Zr (0.01–0.1) and V/Sc (6.1–8) ratios.

5 | DISCUSSION

5.1 | Biogenicity of mat fragments and acritarchs

Some of the sedimentary features reported above are consistent with physical mat destruction, based on (i) easy

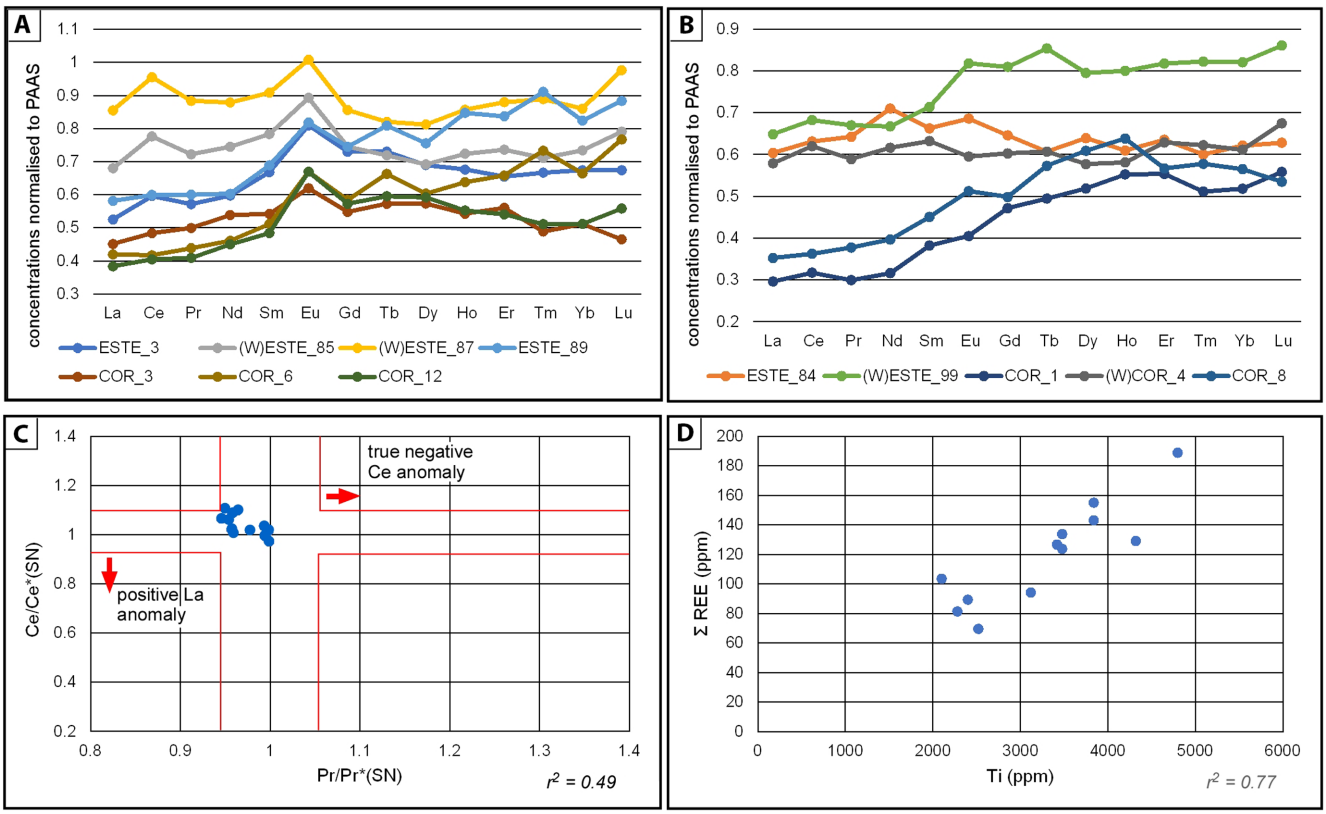

FIGURE 7 Geochemical diagrams for selected greywackes of the Cíjara Formation from the banks of the Estenilla (acronym ESTE) and Alagón (COR) rivers; samples from wrinkle interlaminae prefixed (*W*). (A) Shale-normalised (PAAS) REE patterns exhibiting a distinct positive CE anomaly. (B) Similar patterns lacking Ce anomalies. (C) Plot of $Ce_{(SN)}$ versus $Pr_{(SN)}$ anomalies (after Bau & Dulski, 1996) showing the absence of true Ce anomalies (coefficient of correlation, $r^2 = 0.49$). (D) Plot of Ti versus ΣREE showing a strong positive correlation ($r^2 = 0.77$).

scour and tear of mat surfaces, (ii) flexible behaviour of mat fragments during transport, illustrated by their rolled-up aspect and (iii) the trapping of mica flakes displaying random orientations, a result of their embedding within extracellular polymeric substances (EPS; Schieber et al., 2007).

Raman spectra of AOM and extracted 'bacteriomorph acritarchs' have yielded further data for interpretation (see representative spectra in Figure 5A,B,C). The AOM consists of any kind of structureless organic components at the microscopic scale, which commonly incorporate pyritic inclusions. The organic matter residue obtained after acid treatment of the Cíjara greywacke interbeds is mainly amorphous (in palynological slides, organic matter is composed of 60–68% AOM) with some figured components, represented by 'bacteriomorph acritarchs'. The latter become abundant after maceration in some homogeneous shales. The AOM within wrinkle structures (greywackes) and the individualised acritarchs extracted from the claystone matrix show identical RAMAN results. The transition from acritarchs to AOM show different degrees of degradation features, reflecting intermediate stages to completely degraded organic matter (Tyson, 1995).

In natural carbonaceous material, well-organised graphite is Raman active at 1580 cm^{-1} (G band). In disordered and poorly organised organic matter, the G band splits into two peaks: 1600 cm^{-1} (G band) and 1350 cm^{-1} (D1 band), the latter with a shoulder (D2 band) at 1620 cm^{-1} (Wopenka & Pasteris, 1993). Supplementary bands can form shoulders on the D1 band at 1500 cm^{-1} and 1190 to 1250 cm^{-1}, named D3 and D4 band, respectively, when the crystallinity of the carbonaceous material is low (Lahfid et al., 2010). Spectra of the Cíjara AOM display distinct G and D1 bands, punctuated by additional peaks that reflect the presence of associated minerals, which show the typical CO_3^{2-} vibration modes υ1 (1085 cm^{-1}), υ3 (1435 cm^{-1}) and υ4 (711 cm^{-1}) of calcite; υ1 (1097 cm^{-1}), υ3 (1443 cm^{-1}) and υ4 (725 cm^{-1}) of dolomite; and υ1 (1090 cm^{-1}), υ3 (1442 cm^{-1}) and υ4 (738 cm^{-1}) of siderite (Frezzotti et al., 2012), a micritic component embedded in organic matter that, in this case study, can be exclusively determined by SEM and Raman spectroscopy. In contrast, spectra of individual acritarchs display well-developed D3 and D4 bands, have a D2 band unseparated from the G band, a broad D1 band and an intensity ratio I_{D1}/I_G lower than 1. These features are typical of spectra of poorly ordered organic matter (Kouketsu et al., 2014; Sauerer et al., 2017), and fit well with other Raman analyses made in Neoproterozoic acritarchs (Baludikay et al., 2018).

There is no significant difference in the band positions between spectra acquired on extracted 'bacteriomorph acritarchs' and AOM on thin sections. However, spectra acquired on specimens of *B. faveolata* and *P. caurensis*, after applying the baseline subtraction protocol, display the most significant RAMAN bands, despite some slight shifts towards lower values for the width and the intensity of well-known bands. The relative intensities and shapes of the D and G bands provide quantification for assessing the level of order (crystalline carbon) compared to disorder (amorphous carbon). The nearly equal intensities of the D and G bands are comparable to Raman spectra for disordered graphite and amorphous carbon (Merlen et al., 2017). The width of the G peak is useful in order to analyse the degree of disorder of the sample: the higher the disorder, the higher the width (Ferrari & Robertson, 2000). Raman analyses were performed at different magnifications of organic matter displaying different degrees of preservation. At low magnification (spatial resolution of *ca* 5 μm), the G peak is almost negligible (*a* in Figure 5A). The potential for more accurate spatially resolved analysis was explored with a high-resolution Raman analysis (spatial resolution *ca* 1 μm; *b–e* in Figure 5A). The D and G bands become distinct and their intensity increase in better preserved amorphous organic material. The rise in the D band intensity would reflect the increase in the concentration of nanometre-sized polyaromatic structures in the volume of material explored by the laser (at about 1 μm^3) and a notable growth in the extent of the polyaromatic sheets. The D band intensity reaches a maximum when the carbon is completely polyaromatic (Rouzaud et al., 2015). Upon increasing organic material decomposition and oxidative weathering, aliphatic chains are removed and oxygenated functional groups and their sulphur and nitrogen equivalents are released (Marshall et al., 2010). Therefore, the presence of different Raman spectral shapes in each sample can be interpreted as the coexistence of in situ and reworked materials and/or of different particles of organic matter.

Biomarkers considered to be characteristic for cyanobacteria and potentially suited for tracing cyanobacterial blooms in modern and past ecosystems include mid-chain branched alkanes, C-2 methylated bacteriohopanepolyols (BHPs) as well as their diagenetic products, and BHP structures (such as C-30, 32, 33, 34, 35-pentol BHP) only observed in cyanobacteria to date. While 2Me-BHPs are produced by cyanobacteria (Talbot et al., 2008), the gene responsible for BHP methylation at the C-2 position has been identified in a wide range of other bacterial phyla (Welander et al., 2010), suggesting further sources. The C-2 methylation would increase rigidity to bacterial membranes during episodes of stress (Wu et al., 2015).

In addition, the PUFAs 18:2ω6, 18:3ω6 and 18:4ω3 have been reported in high abundances in certain genera of both unicellular as well as filamentous heterocystous cyanobacteria. Pure cultures of cyanobacteria are generally

characterised by relatively simple cellular FA distributions dominated by 16:0, 16:1ω9, 18:2ω6 or 18:3ω3 (Bauersachs et al., 2017; Summons et al., 1996; Talbot et al., 2008; Vargas et al., 1998).

The alkanes 17:1 and 7-methyl-heptadecane, yielded by the samples, are typical compounds in cyanobacteria (Bauersachs et al., 2017; Berndmeyer et al., 2014; Kaiser et al., 2020; Liu et al., 2013). There was a remarkable presence of palmitic acid (16:0), together with MUFAs (18:1ω7, 16:1ω7) and PUFAs (18:2ω6, 18:3ω6), which are well-known biomarkers of cyanobacteria and phytoplankton (Bauersachs et al., 2017; Napotalino, 1999). It is remarkable that samples showed abundant monosaccharides, mainly hexoses, such as mannose, glucose and galactose, as well as arabinose, which belongs to the group of pentoses. Pentoses and hexoses are sugar moieties that are part of heterocyst glycolipids (HGs), which are biomarkers for cyanobacteria that use heterocysts to carryout N_2 fixation (Bauersachs et al., 2009; Gambacorta et al., 1999). The sugar moiety of HGs found in free-living heterocystous cyanobacteria is typically hexose, while the HGs associated with endosymbiotic heterocystous cyanobacteria in diatom–diazotroph associations (cyanobacteria symbiotic with diatoms) contain a pentose moiety (Bale et al., 2019; Schouten et al., 2013). In this regard, hexose HGs have been applied as specific biomarkers for the presence of N_2-fixing cyanobacteria in marine and lacustrine geological records (Bale et al., 2019; Bauersachs et al., 2010; Sollai et al., 2017). Based on biomarker analyses, 'bacteriomorph acritarchs' may be assigned to cyanobacteria.

5.2 | Environmental controls

The preservation of the Cíjara wrinkle structures is directly linked to the reddened aspect of their laminae reflecting the original precipitation of iron-rich sulphides, subsequently transformed into iron oxyhydroxides (Figure 4B through F). The onset of wrinkle structures associated with hardgrounds punctuating the aforementioned shoaling-upward cycles suggest the episodic colonisation of greywacke/sandy shoals by microbial biofilms and mats, evidencing episodes in which the bedform ceased to migrate. However, the most distinct preservation of microbial mats is related to redeposited material as deformed and rolled-up mat (allochthonous) fragments. Decreased energy episodes in migrating sandy shoals, associated with ironstone horizons would be, therefore, potentially recognisable by the preservation of rafted fragments of former microbial mats.

There is a noticeable increase in REE-rich phosphate (monazite) and subsidiary metal sulphide crystals underlying some wrinkle interlaminae (Figure 4I through N), which is highlighted by the ΣREE content displayed by these samples (Table S1). This can be interpreted as the potential interplay of three processes: clay binding, microbial biomineralisation and/or trapping and binding:

1. Some REE-rich clays, such as lanthanum modified bentonite (LMB), commercially available as Phoslock™ treatment, can precipitate phosphate by electrostatically binding lanthanum. The LMB clays and other modified zeolites comprise several adsorption sites that favour the precipitation of stable minerals, such as monazite ($LaPO_4$). However, La^{3+} binding by dissolved organic carbon (DOC) hinders La-phosphate precipitation (Dithmer et al., 2016; Neweshy et al., 2022), which would restrict its application in this case study.
2. Some microorganisms have the ability to adsorb REE ions and convert them to metal nanocrystals. The concentration of monazite lining the base of some wrinkle interlaminae suggest microbial biosorption, a result of which would be the gradual transformation of REE ions to phosphate minerals on microbial cell surfaces (e.g. Ce can be transformed into $CePO_4$ within 5 days under 120°C hydrothermal conditions by the bacterium *Bacillus licheniformis*; Cheng et al., 2022). Phosphate groups are dominant sorption sites of REE ions onto the surface of some microorganisms with exopolysaccharides efficient in binding heavy metal ions (Moriwaki et al., 2013), such as *Phormidium* and *Anabaena* filamentous cyanobacteria (Fischer et al., 2019; Kim et al., 2011). The complexation of lanthanum with bacterially derived phosphate groups has been achieved in the laboratory, facilitating La nucleation and precipitation as crystalline minerals. Some bacteria, such as *B. licheniformis*, can mediate lanthanum transformation from amorphous compounds to stable monazite nanocrystals (Cheng et al., 2018).
3. Another possibility to explain the association of monazite with metal sulphides is the binding and trapping function of biofilms and mats for detrital heavy grains, which would be incorporated into the microbial laminae. Biostabilisation of grainy substrates by binding and trapping, EPS-mediated concentration of heavy grains (Lan et al., 2021; Tice et al., 2011; Wang et al., 2021), and microbially induced precipitation of monazite must be distinguished from diagenetic features related to 'mat decay mineralisation' responsible for the precipitation of reducing minerals, such as pyrite, siderite and ankerite.

Is the active biosorption versus biostabilisation of REE-rich phosphate and subsidiary metal sulphide grains related to anoxic conditions controlled by organic matter biodegradation? As reported in Section 4.7, the light to

heavy REE ratios (from wrinkle-bearing and wrinkle-free greywacke samples) were assessed by the La_N/Yb_N and $Pr_{(SN)}/Yb_{(SN)}$ fractionation indexes, two expressions of the relative enrichment of HREE over LREE values, which ranges from 0.57 to 0.98 and 0.58 to 1 respectively. These ranges indicate that LREE are moderately to non-depleted in favour of HREE. Nearly all the samples contain slight positive shale-normalised Eu anomalies (Eu/Eu* = 0.96–1.3), an enrichment distinctly illustrated in Figure 7A. This slight anomaly may reflect both the input of plagioclase from the neighbouring arc-related source, and the influence of the synsedimentary hydrothermal activity, as shown by the common presence of contemporaneous hydrothermal dykes that behaved as sources for ubiquitous vein quartz clasts (Álvaro et al., 2019).

Anomalies of Ce are of particular interest, because they can record redox conditions in the overlying water column and during early diagenesis. True Ce anomalies are monitored in a plot of Ce/Ce* versus Pr/Pr* (Bau & Dulski, 1996). As their ratios are close to unity, neither Ce nor Pr anomalies are recorded in the greywacke host rock. Finally, other indicators of redox conditions imply oxic conditions for the Cíjara greywacke substrata, such as the U/Th (<1.25; McKay et al., 2007), V/Cr (<2; Madukwe, 2016) and V/Sc (<9.1; Hetzel et al., 2009) ratios, and even the Ni/Co ratio for the source area's redox state (<5; Jones & Manning, 1994). Therefore, organic matter degradation and mat decomposition should not be associated with dysoxic to anoxic substrata of the Cíjara Formation (precluded by REE redox indicators), but to diagenetic processes and/or weathering oxidation (Pacton et al., 2011).

5.3 | Preservation of Ediacaran cyanobacterial blooms

Extraction of organic matter from the Cíjara wrinkle structure samples by acid maceration has confirmed the presence of two 'acritarch bacteriomorphs', *B. faveolata* and *P. cauriensis*, as previously reported by Palacios Medrano (1989) and Sequeira (2011) from interbedded homogeneous shales. *Bavlinella faveolata* occurs as spherical individuals, ranging in diameter from 5 to 28 μm, composed of subspherical cells ranging from 0.5 to 3 μm in size, packed together in a raspberry-like multisphere (Figure 8A,C). A dense external crown is commonly observed. In thin section, the nucleus is either distinct or somewhat collapsed, suggesting the presence of a hollow interior (Palacios Medrano, 1989). The species is highly abundant in the Cíjara greywackes of the Estenilla stratotype locally reaching monospecific densities of up to 28×10^5 specimens/g after acid maceration (Palacios Medrano, 1989). In contrast, the endemic *P. cauriensis* are spherical capsules, 2 to 20.8 μm in diameter, with reticulate to microreticulate ornamentation and a radial arrangement of elongated vesicles around its inner core (Figure 8B,D). *Palaeogomphosphaeria cauriensis* is less abundant than *B. faveolata*, reaching about 80 specimens per 10 g in the Alagón section and becoming anecdotic in the Estenilla section (Palacios Medrano, 1989). Both species occur as solitary specimens or arranged in clusters. Single unicells, dyads and aggregates would represent both different stages in the life cycle of each taxon and progressive degradation by bacterial activity.

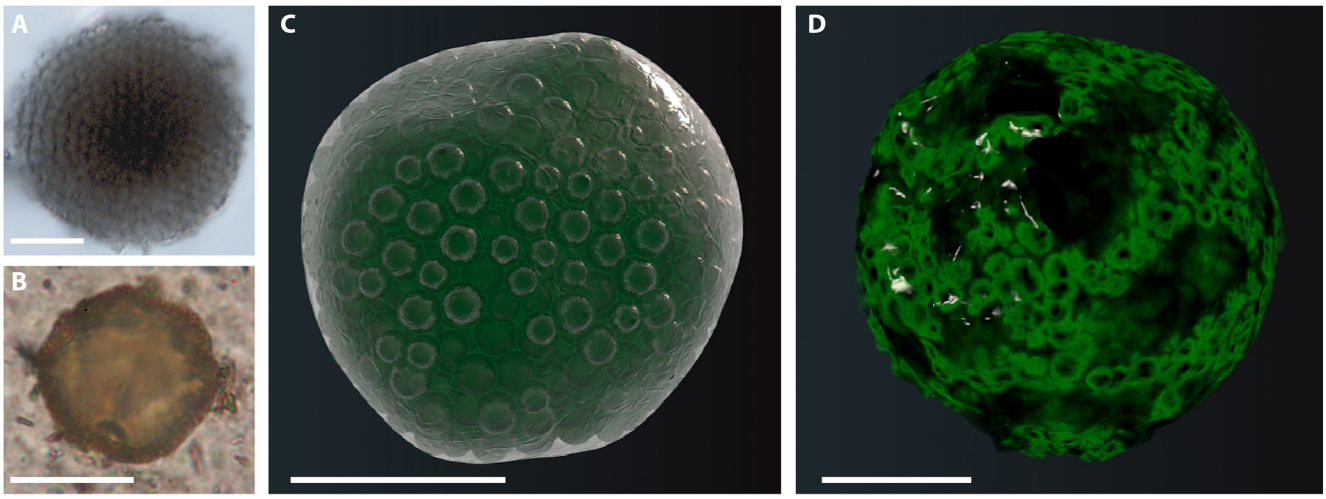

FIGURE 8 Light microscopy photomicrographs of representative bacteriomorph acritarch (cyanobacterial) microfossils preserved in MISS-bearing greywackes of the Ediacaran Cíjara Formation. (A) *Bavlinella faveolata* Shepeleva, 1962 from the Cíjara stratotype. (B) *Palaeogomphosphaeria cauriensis* Palacios Medrano, 1989 from the Alagón river bank section. (C) Three-dimensional (3D) model of *B. faveolata* using CINEMA 4D Studio R14 software and based on specimens illustrated by Palacios Medrano (1989). (D) 3D model of *P. cauriensis*; scale bar = 10 μm.

Bavlinella faveolata is a cosmopolitan acritarch species, which first occurred in Cryogenian strata. Late Ediacaran plankton commonly contains *Bavlinella*-dominated acritarch assemblages, even contemporaneously with the Marinoan Snowball glaciation (Gaucher & Sprechmann, 1999). Massive occurrence of *B. faveolata*-dominant (nearly monospecific) assemblages reflects microbial blooms related to the eutrophication of vast oceanic areas. They have been reported, among others, in Svalbard, North America, Norway, Namibia, China, Czech Republic, Uruguay, Brazil, India and Urals (Chiglino et al., 2015; Gaucher et al., 2005, 2008; Prasad et al., 2010; Vavrdová, 2008; Yin & Yuan, 2007).

A modern analogue of *Bavlinella* is the bloom-forming, planktonic cyanobacterium *Microcystis*, able to outcompete and even exclude eukaryotic plankton assemblages in high-nutrient (eutrophic) waters. This is due to their more efficient use of nutrients, generation of potent toxins and/or generation of water column anoxia (Frei et al., 2013; Mansuy & Vidal, 1983; Nasri et al., 2007). If large areas of the Ediacaran oceans became eutrophic, mainly linked to the increase of nitrogen and phosphorous fluxes in upwelling marine systems, such as those reported in the Cadomian retroarc basin preserved in the Iberian margin of West Gondwana (Álvaro et al., 2016), *Bavlinella* productivity blooms may have effectively decimated a large part of the eukaryotic plankton (Quiblier et al., 2013; She et al., 2014). Development of massive growth episodes of cyanobacteria (cyanoblooms) has been reported in many present-day eutrophic to hypertrophic lakes, and epeiric and semi-enclosed seas, such as the Baltic Sea (Munkes et al., 2021; Rastogi et al., 2015). The geographic semi-enclosed condition of the present-day Baltic Sea would be similar to the palaeogeographical configuration of the Cadomian retroarc basin reported in this paper, sandwiched between an active Cadomian arc to the south-west and West Gondwana to the north-east.

As reported above, the Raman peaks and biomarkers yielded by the benthic mat fragments and 'bacteriomorph acritarchs' encased in wrinkle structures, as well as the pelagic acritarchs embedded in some shale interbeds (deposited from the water column by decantation) are the same. Should we infer that the bloom-forming *B. faveolata* cyanobacterium was responsible for both pelagic populations and benthic development of microbial mats? The ability of some cyanobacteria (e.g. *Microcystis*) to form pelagic blooms and benthic mats is commonly related to adaptations to seasonal changes. Its life cycle includes a planktic bloom phase during summer intervals in the water column, but the colonies sink in winter, reach the sediment and develop a physiological rest adaptation as the poor light conditions restrict photosynthetic activity (Brunberg & Blomqvist, 2002; Latour et al., 2004).

The benthic survival of *Microcystis* colonies in temperate waters has frequently been classified as 'overwintering'. Long-term laboratory incubations have shown that colonies are able to restart growth even after extended time spans of benthic resting. In eutrophic lakes and estuaries, the benthic biomass may substantially exceed the maximum planktic biomass, thus indicating that *Microcystis* benthic colonies are able to survive for longer periods. Overwintering populations subsequently inoculate the water column in spring and promote the development of dense surface blooms of *Microcystis* during summer, when the buoyancy state is regulated by light (Verspahen et al., 2004; Visser et al., 1995). Some green algae, such as *Picocystis*, are also known to inhabit both surface and deep habitats, even when oxygen is below detection (Stamps et al., 2018).

The role of acritarchs and other palynomorphs as major constituents of Proterozoic microbial mats has been previously reported, among others, in Mesoproterozoic black shales from the Taoudeni Basin in Mauritania (Blumenberg et al., 2012), Neoproterozoic turbidites and biolaminated siltstones of the Officer Basin (Arouri et al., 2000) and the Centralian Superbasin (Logan et al., 1999) in Australia, or late Ediacaran silty mats of Finland (Willman & Slater, 2021), offering a direct body-fossil insight into mat-forming microbial communities.

6 | CONCLUSIONS

Raman spectra measured on cyanobacterial acritarchs and their AOM, in both extracted kerogen from homogeneous shales and in situ thin sections of microbial mat fragments encased in wrinkle structures from the Ediacaran Cíjara Formation (Central Iberian Zone, Spain), allowed both the biogenicity of their encased mat fragments and 'bacteriomorph acritarchs' to be evaluated, together with their associated REE-rich phosphate (monazite) and subsidiary metal sulphide crystals. The presence of well-known biomarkers of cyanobacteria in wrinkle-bearing greywackes, specifically the alkanes 17:1 and 7-methyl-heptadecane together with the saturated FAs 16:0, the unsaturated FAs 18:1ω7, 16:1ω7, 18:2ω6 and 18:3ω6, and hexoses and pentoses which are sugar moieties that are part of HGs, revealed the biogenicity of their allochthonous mat fragments. Wrinkle structures are associated with reddened hardgrounds punctuating shoaling-upward cycles that reflect the episodic colonisation and subsequent reworking of microbial biofilms and mats encrusting sandy/greywacke shoals. Cyanobacterial bloom-forming *Bavlinella* remains are

extremely abundant and nearly monospecific, and represent eutrophic episodes in a semi-enclosed retroarc basin sandwiched between an active Cadomian arc and West Gondwana.

ACKNOWLEDGEMENTS

The authors warmly appreciate the constructive criticism made by two anonymous reviewers, E. Samankassou for technical editing, Sílvia Ribeiro Fonseca and Pedro Silva (Escola Superior de Tecnologia, Instituto Politécnico de Castelo Branco) for digital reconstruction of acritarchs, and Laura Tormo (MNCN) for her analytical skills. This paper is a contribution to Spanish Project PID2021-125585NB-I00.

CONFLICT OF INTEREST STATEMENT

The authors have no conflict of interest to declare.

DATA AVAILABILITY STATEMENT

Data sharing is not applicable to this article as no new data were created or analyzed in this study.

ORCID

J. Javier Álvaro https://orcid.org/0000-0001-6294-1998

REFERENCES

Allwood, A.C., Walter, M.R. & Marshal, C.P. (2006) Raman spectroscopy reveals thermal palaeoenvironments of c. 3.5 billion-year-old organic matter. *Vibrational Spectroscopy*, 41, 190–197.

Álvaro, J.J., Cortijo, I., Jensen, S., Lorenzo, S., Palacios, T. & Pieren, A. (2019) Updated stratigraphic framework and biota of the Ediacaran and Terreneuvian in the Alcudia-Toledo Mountains, Central Iberian Zone, Spain. *Estudios Geológicos*, 75(2), e093.

Álvaro, J.J. & Lorenzo, S. (2022) Cadomian orogenic collapse in the Ibor and Alcudia anticlines of the Central Iberian Zone, Spain. *Geological Magazine*, 159, 1251–1261.

Álvaro, J.J., Shields, G.A., Ahlberg, P., Jensen, S. & Palacios, T. (2016) Ediacaran–Cambrian phosphorites from the western margins of Gondwana and Baltica. *Sedimentology*, 63, 350–377.

Arouri, K., Conaghan, P.J., Walter, M.R., Bischoff, G.C.O. & Grey, K. (2000) Reconnaissance sedimentology and hydrocarbon biomarkers of Ediacaran microbial mats and acritarchs, lower Ungoolya Group, Officer Basin. *Precambrian Research*, 100, 235–280.

Bale, N.J., Hennekam, R., Hopmans, E.C., Dorhout, D., Reichart, G.J., van der Meer, M., Villareal, T.A., Sinninghe Damsté, J.S. & Schouten, S. (2019) Biomarker evidence for nitrogen-fixing cyanobacterial blooms in a brackish surface layer in the Nile River plume during sapropel deposition. *Geology*, 47, 1088–1092.

Baludikay, B.K., François, C., Sforna, M.C., Beghin, J., Cornet, Y., Storme, J.Y., Fagel, N., Fontaine, F., Littke, R., Baudet, D., Delvaux, D. & Javaux, E.J. (2018) Raman microspectroscopy, bitumen reflectance and illite crystallinity scale: comparison of different geothermometry methods on fossiliferous Proterozoic sedimentary basins (DR Congo, Mauritania and Australia). *International Journal of Coal Geology*, 191, 80–94.

Bau, M. & Dulski, P. (1996) Distribution of yttrium and rare-earth elements in the Penge and Kuruman Iron-Formations, Transvaal Supergroup, South Africa. *Precambrian Research*, 79, 35–55.

Bauersachs, T., Compaoré, J., Hopmans, E.C., Stal, L.J., Schouten, S. & Sinninghe Damsté, J.S. (2009) Distribution of heterocyst glycolipids in cyanobacteria. *Phytochemistry*, 70, 2034–2039.

Bauersachs, T., Speelman, E.N., Hopmans, E.C., Reichart, G.J., Schouten, S. & Sinninghe Damsté, J.S. (2010) Fossilized glycolipids reveal past oceanic N_2 fixation by heterocystous cyanobacteria. *Proceedings of the National Academy of Sciences of the United States of America*, 107, 19190–19194.

Bauersachs, T., Talbot, H.M., Sidgwick, F., Sivonen, K. & Schwark, L. (2017) Lipid biomarker signatures as tracers for harmful cyanobacterial blooms in the Baltic Sea. *PLoS One*, 12(10), e086360.

Bayet-Goll, A. & Daraei, M. (2020) Palaeoecological, sedimentological and stratigraphical insights into microbially induced sedimentary structures of the lower Cambrian successions of Iran. *Sedimentology*, 67, 3199–3235.

Berndmeyer, C., Thiel, V., Schmale, O., Wasmund, N. & Blumenberg, M. (2014) Biomarkers in the stratified water column of the Landsort Deep (Baltic Sea). *Biogeosciences*, 11, 7009–7023.

Beyssac, O., Goffé, B., Chopin, C. & Rouzaud, J.N. (2002) Raman spectra of carbonaceous material in metasediments: a new geothermometer. *Journal of Metamorphic Geology*, 20, 859–871.

Blumenberg, M., Thiel, V., Riegel, W., Kah, L.C. & Reitner, J. (2012) Biomarkers of black shales formed by microbial mats, Late Mesoproterozoic (1.1 Ga) Taoudeni Basin, Mauritania. *Precambrian Research*, 196-197, 113–127.

Brunberg, A.K. & Blomqvist, P. (2002) Benthic overwintering of *Microcystis* colonies under different environmental conditions. *Journal of Plankton Research*, 24, 1247–1252.

CASEM (Committee on an Astrobiology Strategy for the Exploration of Mars). (2007) *An Astrobiology strategy for the exploration of Mars*. Washington, DC: The National Academies Press.

Catelani, T., Pratesi, G. & Zoppi, M. (2014) Raman characterization of ambient airborne soot and associated mineral phases. *Aerosol Science and Technology*, 48, 13–21.

Cheng, Y.J., Zhang, L., Bian, X.J., Zuo, H.Y. & Dong, H.K. (2018) Adsorption and mineralization of REE—lanthanum onto bacterial cell surface. *Environmental Science and Pollution Research*, 25, 22334–22339.

Cheng, Y.J., Zhang, T.T., Zhang, L., Ke, Z.B., Kovarik, L. & Dong, H.L. (2022) Resource recovery: adsorption and biomineralization of cerium by *Bacillus licheniformis*. *Journal of Hazardous Materials*, 426, 127844.

Chiglino, L., Gaucher, C., Sial, A.N. & Ferrerira, V.P. (2015) Acritarchs of the Ediacaran Frecheirinha Formation, Ubajara Group, Northeastern Brazil. *Anais da Academia Brasileira de Ciencias*, 87, 635–649.

Davies, N.S., Liu, A.G., Gibling, M.R. & Miller, R.F. (2016) Resolving MISS conceptions and misconceptions: a geological approach to sedimentary surface textures generated by microbial and abiotic processes. *Earth-Science Reviews*, 154, 210–246.

Dithmer, L., Nielsen, U.G., Lürling, M., Spesrs, B.M., Yasseri, S., Lundberg, D., Moore, A., Jensen, N.D. & Reitzel, K. (2016) Responses in sediment phosphorous and lanthanum concentrations and composition across 10 lakes following applications of lanthanum modified bentonite. *Water Research*, 97, 101–110.

Ferrari, A.C. & Robertson, J. (2000) Interpretation of Raman spectra of disordered and amorphous carbon. *Physical Review B*, 61, 14095–14107.

Fischer, C.B., Körsten, S., Rösken, L.M., Cappel, F., Beresko, C., Ankerhold, G., Schönleber, A., Geimer, S., Ecker, D. & Wehner, S. (2019) Cyanobacterial promoted enrichment of rare earth elements europium, samarium and neodymium and intracellular europium particle formation. *RSC Advances*, 9, 32581–32593.

Foucher, F., Ammar, M.R. & Westall, F. (2015) Revealing the biotic origin of silicified Precambrian carbonaceous microstructures using Raman spectroscopic mapping, a potential method for the detection of microfossils on Mars. *Journal of Raman Spectroscopy*, 46, 873–879.

Frei, R., Gaucher, C., Dtolper, D. & Canfield, D.E. (2013) Fluctuations in late Neoproterozoic atmosphere oxidation—Cr isotope chemostratigraphy and iron speciation of the late Ediacaran lower Arroyo del Soldado Group (Uruguay). *Gondwana Research*, 23, 797–811.

Frezzotti, M.L., Terce, F. & Casagli, A. (2012) Raman spectroscopy for fluid inclusion analysis. *Journal of Geochemical Exploration*, 112, 1–20.

Gambacorta, A., Trincone, A., Soriente, A. & Sodano, G. (1999) Chemistry of glycolipids from the heterocysts of nitrogen-fixing cyanobacteria. *Current Topics in Phytochemistry*, 2, 145–150.

Gaucher, C., Blanco, G., Chiglino, L., Poire, D.G. & Germs, G. (2008) Acritarchs of Las Ventanas Formation (Ediacaran, Uruguay); implications for the timing of coeval rifting and glacial events in western Gondwana. *Gondwana Research*, 13, 488–501.

Gaucher, C., Frimmel, H.E. & Germs, G.J.B. (2005) Organic-walled microfossils and biostratigraphy of the upper Port Nolloth Group (Namibia): implications for latest Neoproterozoic glaciations. *Geological Magazine*, 142, 539–559.

Gaucher, C. & Sprechmann, P. (1999) Upper Vendian skeletal fauna of the Arroyo del Soldado Group, Uruguay. *Beringeria*, 23, 55–91.

Hackley, P.C., Jubb, A.M., McAleer, R.J., Valentine, B.J. & Birdwell, J.E. (2021) A review of spatially resolved techniques and applications of organic petrography in shale petroleum systems. *International Journal of Coal Geology*, 241, 103745.

Hetzel, A., Böttcher, M.E., Wortman, U.G. & Brumsack, H.J. (2009) Paleo-redox conditions during OAE 2 reflected in Demerara Rise sediment geochemistry (ODP Leg 207). *Palaeogeography*, 273, 820–829.

Hutchinson, I.B., Ingley, R., Edwards, H.G.M., Harris, L., McHugh, M., Malherbe, C. & Parnell, J. (2014) Raman spectroscopy on Mars: identification of geological and bio-geological signatures in Martian analogues using miniaturized Raman spectrometers. *Philosophical Transactions of the Royal Society A: Mathematical, Physical and Engineering Sciences*, 372, 20140204.

Jensen, S. & Palacios, T. (2016) The Ediacaran–Cambrian trace fossil record in the Central Iberian Zone, Iberian peninsula. *Comunicações Geologicas*, 103, 83–92.

Jones, B. & Manning, D.A.C. (1994) Comparison of geochemical indices used for the interpretation of palaeoredox conditions in ancient mudstones. *Chemical Geology*, 111, 111–129.

Kaiser, J., Wasmund, N., Kahru, M., Wittenborn, A.K., Hansen, R., Häusler, K., Moros, M., Schulz-Bull, D. & Arz, H.W. (2020) Reconstructing N_2-fixing cyanobacterial blooms in the Baltic Sea beyond observations using 6- and 7-methylheptadecane in sediments as specific biomarkers. *Biogeosciences*, 17, 2579–2591.

Kim, J.A., Dodbiba, G., Tanimura, Y., Mitsuhashi, K., Fukuda, N., Okaya, K., Matsuo, S. & Fujita, T. (2011) Leaching of rare-earth elements and their adsorption by using blue-green algae. *Materials Transactions*, 52, 1799–1806.

Kouketsu, Y., Mizukami, T., Mori, H., Endo, S., Aoya, M., Hara, H., Nakamura, D. & Wallis, S. (2014) A new approach to develop the Raman carbonaceous material geothermometer for low-grade metamorphism using peak width. *Island Arc*, 23, 33–50.

Lahfid, A., Beyssac, O., Deville, E., Negro, F., Chopin, C. & Goffé, B. (2010) Evolution of the Raman spectrum of carbonaceous material in low-grade metasediments of the Glarus Alps (Switzerland). *Terra Nova*, 22, 354–360.

Lan, J., Zhang, S., Dong, Y., Li, J., Li, S., Feng, L. & Hou, H. (2021) Stabilization and passivation of multiple heavy metals in soil facilitating by pinecone-based biochar: mechanisms and microbial community evolution. *Journal of Hazardous Materials*, 420, 126588.

Latour, D., Sabido, O., Salençon, M.J. & Giraudet, H. (2004) Dynamics and metabolic activity of the benthic cyanobacterium *Microcystis aeruginosa* in the Grangent reservoir (France). *Journal of Plankton Research*, 26, 719–726.

Linnemann, U., Pieren, A., Hofmann, M., Drost, K., Quesada, C., Axel, G., Marko, L., Gärtner, A., Zieger, J., Ulrich, J., Krause, R., Vickers-Rich, P. & Horak, J. (2018) A ~565 Ma old glaciation in the Ediacaran of peri-Gondwanan West Africa. *International Journal of Earth Sciences*, 107, 885–911.

Liu, A., Zhu, T., Lu, X. & Song, L. (2013) Hydrocarbon profiles and phylogenetic analyses of diversified cyanobacterial species. *Applied Energy*, 111, 383–393.

Logan, G.A., Calver, C.R., Gorjan, P., Summons, R.E., Hayes, J.M. & Walter, M.R. (1999) Terminal Proterozoic mid-shelf benthic microbial mats in the Centralian Superbasin and their environmental significance. *Geochimica et Cosmochimica Acta*, 63, 1345–1358.

Madukwe, H.Y. (2016) Granulometric analysis of sandstone facies of the Ise Formation, Southwestern Nigeria. *Journal of Multidisciplinary Engineering Science and Technology*, 3, 3909–3919.

Mansuy, C. & Vidal, G. (1983) Late Proterozoic Brioverian microfossils from France: taxonomic affinity and implications of plankton productivity. *Nature*, 302, 606–607.

Mariotti, G., Pruss, S.B., Perron, J.T. & Bosak, T. (2014) Microbial shaping of sedimentary wrinkle structures. *Nature Geoscience*, 7, 736–740.

Marshall, C.P., Edwards, H.G.M. & Jehlicka, J. (2010) Understanding the application of Raman spectroscopy to the detection of traces of life. *Astrobiology*, 10, 229–248.

Mastandrea, A., Perri, E., Russo, F., Spadafora, A. & Tucker, M. (2006) Microbial primary dolomite from a Norian carbonate platform: northern Calabria, southern Italy. *Sedimentology*, 53, 465–480.

McCollom, T.M. & Seewald, J.S. (2006) Carbon isotope composition of organic compounds produced by abiotic synthesis under hydrothermal conditions. *Earth and Planetary Science Letters*, 243, 74–84.

McKay, J.L., Pedersen, T.F. & Mucci, A. (2007) Sedimentary redox conditions in continental margin sediments (NE Pacific)-influence on the accumulation of redox-sensitive trace metals. *Chemical Geology*, 238, 180–196.

McLoughlin, N., Wilson, L.A. & Brasier, M.D. (2008) Growth of synthetic stromatolites and wrinkle structures in the absence of

microbes – implications for the early fossil record. *Geobiology*, 6, 95–105.

Menon, L.R., McIlroy, D., Liu, A.G. & Brasier, M.D. (2016) The dynamic influence of microbial mats on sediments: fluid escape and pseudofossil formation in the Ediacaran Longmyndian Supergroup, UK. *Journal of the Geological Society*, 173, 177–185.

Merlen, A., Buijnsters, J.G. & Pardanaud, C. (2017) A guide to and review of the use of multiwavelength Raman spectroscopy for characterizing defective aromatic carbon solids: from graphene to amorphous carbons. *Coatings*, 7, 153.

Moorman, M. (1974) Microbiota of the late Proterozoic Hector Formation, southwestern Alberta, Canada. *Journal of Paleontology*, 48, 524–539.

Moriwaki, H., Kolde, R., Yoshikawa, R., Warabino, Y. & Yamamoto, H. (2013) Adsorption of rare earth ions onto the cell walls of wild-type and lipoteichoic acid-defective strains of *Bacillus subtilis*. *Applied Microbiology and Biotechnology*, 97, 3721–3728.

Munkes, B., Löptien, U. & Dietze, H. (2021) Cyanobacteria blooms in the Baltic Sea: a review of models and facts. *Biogeosciences*, 18, 2347–2378.

Napotalino, G.E. (1999) Fatty acids as trophic and chemical markers in freshwater ecosystems. In: Arts, M.T. & Wainman, B.C. (Eds.) *Lipids in freshwater ecosystems*. New York: Springer, pp. 21–44.

Nasri, H., Bouaicha, N. & Harche, M.K. (2007) A new morphospecies of *Microcystis* sp. forming bloom in the Cheffia Dam (Algeria): seasonal variation of microcystin concentrations in raw water and their removal in full-scale treatment plant. *Environmental Toxicology*, 22, 347–356.

Neweshy, W., Planas, D., Tellier, E., Marsac, R., Demers, M. & Couture, R.M. (2022) Response of sediment phosphorus partitioning to lanthanum-modified clay amendment and porewater chemistry in a small eutrophic lake. *Environmental Sciences: Processes & Impact*, 24, 1494–1507.

Noffke, N. (2009) The criteria for the biogeneicity of microbially induced sedimentary structures (MISS) in Archean and younger, sandy deposits. *Earth-Science Reviews*, 96, 173–180.

Noffke, N. (2021) Microbially induced sedimentary structures in clastic deposits: implication for the prospection for fossil life on Mars. *Astrobiology*, 21, 866–892.

Noffke, N., Beraldi-Campesi, H., Callefo, F., Carmona, N., Cuadrado, D.G., Hickman- Lewis, K., Homann, M., Mitchell, R., Sheldon, N., Westall, F. & Xiao, S. (2022) Treatise online no. 162: Part B, volume 2, Chapter 5: Microbially induced sedimentary structures (MISS). Treatise Online. https://doi.org/10.17161/to.vi.18111

Noffke, N., Beukes, N. & Hazen, R. (2006a) Spatial and temporal distribution of microbially induced sedimentary structures: a case study from siliciclastic storm deposits of the 2.9 Ga old Witwatersrand Supergroup, South Africa. *Precambrian Research*, 146, 35–44.

Noffke, N., Eriksson, K.A., Hazen, R. & Simpson, E.L. (2006b) A new window into Early Archean life: microbial mats in Earth's oldest siliciclastic deposits (3.2 Ga Moodies Group, South Africa). *Geology*, 34, 253–256.

Noffke, N., Gerdes, G., Klenke, T. & Krumbein, W.E. (2001) Microbially induced sedimentary structures—a new category within the classification of primary sedimentary structures. *Journal of Sedimentary Research*, A71, 649–656.

Noffke, N., Hazen, R. & Nhleko, N. (2003) Earth's earliest microbial mats in a siliciclastic marine environment (2.9 Ga Mozaan Group, South Africa). *Geology*, 31, 673–676.

Ortiz, J.E., Torres, T., Delgado, A., Llamas, F.J. & Valle, M. (2010) Palaeoenvironmental changes in the Padul Basin (Granada, Spain) over the last 1 Ma B.P. based on the biomarker content. *Palaeogeography, Palaeoclimatology, Palaeoecology*, 298, 286–299.

Pacton, M., Gorin, G.E. & Vasconcelos, C. (2011) Amorphous organic matter—experimental data on formation and the role of microbes. *Review of Palaeobotany and Palynology*, 166, 253–267.

Palacios Medrano, T. (1989) Microfósiles de pared orgánica del Proterozoico superior (región central de la Península Ibérica). *Memorias del Museo Paleontológico de la Universidad de Zaragoza*, 3, 1–91.

Pasteris, J.D. & Wopenka, B. (2003) Necessary, but not sufficient: Raman identification of disordered carbon as a signature of ancient life. *Astrobiology*, 3, 727–738.

Pourmand, A., Dauphas, N. & Ireland, T.J. (2012) A novel extraction chromatography and MC-ICP-MS technique for rapid analysis of REE, Sc and Y: revising CI-chondrite and post-Archean Australian Shale (PAAS) abundances. *Chemical Geology*, 291, 38–54.

Prasad, B., Asher, R. & Borgohai, B. (2010) Late Neoproterozoic (Ediacaran)–Early Paleozoic (Cambrian) acritarchs from the Marwar Supergroup, Bikaner-Nagaur Basin, Rajasthan. *Journal of the Geological Society of India*, 75, 415–431.

Pratt, B.R. (2021) Kinneyia-type wrinkle structures on sandstone beds: not microbially induced but deformation features caused by synsedimentary earthquakes. *Palaios*, 36, 313–325.

Pratt, B.R. & Ponce, J.J. (2019) Sedimentation, earthquakes, and tsunamis in a shallow, muddy epeiric sea: Grinnell Formation (Belt Supergroup, ca 1.45 Ga), western North America. *Geological Society of America Bulletin*, 131, 1411–1439.

Quiblier, C., Wood, S., Echenique-Subiabre, I., Heath, M., Villeneuve, A. & Humbert, J.F. (2013) A review of current knowledge on toxic benthic freshwater cyanobacteria—ecology, toxin production and risk management. *Water Research*, 47, 5464–5479.

Rastogi, R.P., Madamwar, D. & Incharoensakdi, A. (2015) Bloom dynamics of cyanobacteria and their toxins: environmental health impacts and mitigation strategies. *Frontiers in Microbiology*, 6, 1254.

Rouzaud, J.N., Deldicque, D., Charon, E. & Pageot, J. (2015) Carbons at the heart of questions on energy and environment: a nanostructural approach. *Comptes Rendus Geoscience*, 347, 124–133.

Rull, F., Maurice, S., Hutchinson, I., Moral, A., Perez, C., Diaz, C., Colombo, M., Belenguer, T., Lopez-Reyes, G., Sansano, A., Forni, O., Parot, Y., Striebig, N., Woodward, S., Howe, C., Tarcea, N., Rodriguez, P., Seoane, L., Santiago, A., Rodriguez-Prieto, J.A., Medina, J., Gallego, P., Canchal, R., Santamaría, P., Ramos, G., Vago, J.L. & . (2017) The Raman laser spectrometer for the ExoMars Rover mission to Mars. *Astrobiology*, 18, 627–654.

Sánchez García, T., Chichorro, M., Solá, R., Quesada, C., Álvaro, J.J., Díez Montes, A., Bellido, F., Ribeiro, C., Quesada, C., Dias da Silva, I.F., Quesada, C. & Gómez Barreiro, J. (2019) The Cambrian–Early Ordovician rift stage in the Gondwanan units of the Iberian Massif. In: Quesada, C. & Oliveira, J.T. (Eds.) *The Geology of Iberia: A Geodynamic Approach, Regional Geology, Review Series*, Vol. 2. Heidelberg: Springer, pp. 27–74.

Sauerer, B., Craddock, P.R., Aljohani, M.D., Alsamadony, K.L. & Abdallah, W. (2017) Fast and accurate shale maturity determination by Raman spectroscopy measurement with minimal sample preparation. *International Journal of Coal Geology*, 173, 150–157.

Schieber, J., Bose, P.K., Erikkson, P.G., Banerjee, S., Sarkar, S., Altermann, W. & Catuneanu, O. (Eds.). (2007) Atlas of microbial mat features preserved within the siliciclastic record. In: *Atlases in geosciences*, Vol. 2. Heidelberg: Springer, pp. 1–311.

Schiffbauer, J.D., Wallace, A.F., Hunter, J.L., Kowalewski, M., Bodnar, R.J. & Xiao, S. (2012) Thermally-induced structural and chemical alteration of organic-walled microfossils: an experimental approach to understanding fossil preservation in meta-sediments. *Geobiology*, 10, 402–423.

Schouten, S., Villareal, T.A., Hopmans, E.C., Mets, A., Swanson, K.M. & Sinninghe Damsté, J.S. (2013) Endosymbiotic heterocystous cyanobacteria synthesize different heterocyst glycolipids than free-living heterocystous cyanobacteria. *Phytochemistry*, 85, 115–121.

Sequeira, A.J.D. (2011) Microfossils of Beiras Group (Monfortinho—Salvaterra do extremo, Beira Baixa, Central Portugal). *Comunicações Geologicas*, 98, 55–60.

She, Z.B., Strother, P. & Papineau, D. (2014) Terminal Proterozoic cyanobacterial blooms and phosphogenesis documented by the Doushantuo granular phosphorites II: microbial diversity and C isotopes. *Precambrian Research*, 251, 62–79.

Shepeleva, E.D. (1962) Plant? fossils of unknown taxonomic position from the deposits of the Bavlinskaya Series in the Volga·Urals oil province. *Doklady Akademii nauk—Earth Science Transactions*, 142, 170–171.

Sollai, M., Hopmans, E.C., Bale, N.J., Mets, A., Warden, L., Moros, M. & Sinninghe Damsté, J.S. (2017) The Holocene sedimentary record of cyanobacterial glycolipids in the Baltic Sea: an evaluation of their application as tracers of past nitrogen fixation. *Biogeosciences*, 14, 5789–5804.

Stamps, B.W., Nunn, H.S., Petrushyn, V.A., Oremland, R.S., Miller, L.G., Rosen, M.R., Bauer, K.W., Thompson, K.J., Tookmanian, E.M., Waldek, A.R., Loyd, S.J., Johnson, H.A., Setevenson, B.S., Berelson, W., Corsetti, F.A. & Spear, J.R. (2018) Metabolic capability and phylogenetic diversity of Mono Lake during a bloom of the eukaryotic phototroph *Picocystis* sp. strain ML. *Applied Environmental Microbiology*, 84(21), e01171-18.

Summons, R.E., Jahnke, L.L. & Simoneit, B.R.T. (1996) Lipid biomarkers for bacterial ecosystems: studies of cultured organisms, hydrothermal environments and ancient sediments. In: Bock, G.R. & Goode, J.A. (Eds.) *Evolution of hydrothermal ecosystems on Earth (and Mars?)*. Wiley, Chichester: Novartis Foundation Symposia, pp. 174–194.

Talavera, C., Martínez Poyatos, D. & González Lodeiro, F. (2015) SHRIMP U–Pb geochronological constraints on the timing of the intra–Alcudian (Cadomian) angular unconformity in the Central Iberian Zone (Iberian massif, Spain). *International Journal of Earth Sciences*, 104, 1739–1757.

Talbot, H.M., Summons, R.E., Jahnke, L.L., Cockell, C.S., Rohmer, M. & Farrimond, P. (2008) Cyanobacterial bacteriohopanepolyol signatures from cultures and natural environmental settings. *Organic Geochemistry*, 39, 232–263.

Tice, M.M., Thornton, D.C.O., Pope, M.C., Olszewski, T.D. & Gong, J. (2011) Archean microbial mat communities. *Annual Review of Earth and Planetary Sciences*, 39, 297–319.

Tyson, R.V. (1995) *Sedimentary organic matter: organic facies and palynofacies*. London: Chapman & Hall, p. 615.

Vago, J.L., Westall, F., Pasteur Instrument Teams, Landing Site Selection Working Group, and Other Contributors, Coates, A.J., Jaumann, R., Korablev, O., Ciarletti, V., Mitrofanov, I., Josset, J.L., de Sanctis, M.C., Bibring, J.P., Rull, F., Goesmann, F., Steininger, H., Goetz, W., Brinckerhoff, W., Szopa, C., Raulin, F., Westall, F., Edwards, H.G.M., Whyte, L.G., Fairén, A.G., Bibring, J.P., Bridges, J., Hauber, E., Ori, G.G., Werner, S., Loizeau, D., Kuzmin, R.O., Williams, R.M.E., Flahaut, J., Forget, F., Vago, J.L., Rodionov, D., Korablev, O., Svedhem, H., Sefton-Nash, E., Kminek, G., Lorenzoni, L., Joudrier, L., Mikhailov, V., Zashchirinskiy, A., Alexashkin, S., Calantropio, F., Merlo, A., Poulakis, P., Witasse, O., Bayle, O., Bayón, S., Meierhenrich, U., Carter, J., García-Ruiz, J.M., Baglioni, P., Haldemann, A., Ball, A.J., Debus, A., Lindner, R., Haessig, F., Monteiro, D., Trautner, R., Voland, C., Rebeyre, P., Goulty, D., Didot, F., Durrant, S., Zekri, E., Koschny, D., Toni, A., Visentin, G., Zwick, M., van Winnendael, M., Azkarate, M., Carreau, C. & the ExoMars Project Team. (2017) Habitability on early Mars and the search for biosignatures with the ExoMars rover. *Astrobiology*, 18, 471–510.

Vargas, M.A., Rodríguez, H., Moreno, J., Olivares, H., del Campo, J.A., Rivas, J. & Guerrero, M.G. (1998) Biochemical composition and fatty acid content of filamentous cyanobacteria. *Journal of Phycology*, 34, 812–817.

Vavrdová, M. (2008) Proterozoic acritarchs from the Precambrian–Cambrian transition in southern Moravia. *Bulletin of Geosciences*, 83, 85–92.

Verspahen, J.M.H., Snelder, E.O.F.M., Visser, P.M., Huisman, J. & Mur, L.R. (2004) Recruitment of benthic *Microcystis* (Cyanophyceae) to the water column: internal buoyancy changes or resuspension? *Journal of Phycology*, 40, 260–270.

Visser, P.M., Ibelings, B.W. & Mur, I.R. (1995) Autumnal sedimentation of *Microcystis* spp. as result of an increase in carbohydrate ballast at reduced temperature. *Journal of Plankton Research*, 17, 919–933.

Vodrážková, S., Vodrážka, R., Munnecke, A., Franců, J., Al-Bassam, K., Halodová, P. & Tonarová, P. (2018) Microbially induced wrinkle structures in Middle Devonian siliciclastics from the Prague Basin, Czech Republic. *Lethaia*, 52, 149–164.

Wang, L., Rinklebe, J., Tack, F.M.G. & Hou, D. (2021) A review of green remediation strategies for heavy metal contaminated soil. *Soil Use and Management*, 37, 936–963.

Welander, P.V., Coleman, M.L., Sessions, A.L., Summons, R.E. & Newman, D.K. (2010) Identification of a methylase requires for 2-methylhopanoid production and implications for the interpretation of sedimentary hopanes. *Proceedings of the National Academy of Sciences of the United States of America*, 107, 8537–8542.

Willman, S. & Slater, B.J. (2021) Late Ediacaran organic microfossils from Finland. *Geological Magazine*, 158, 2231–2244.

Wopenka, B. & Pasteris, J.D. (1993) Structural characterization of kerogen to granulite facies graphite: applicability of Raman microprobe spectroscopy. *American Mineralogist*, 78, 533–557.

Wu, C.H., Bialecka-Fornal, M. & Newman, D.K. (2015) Methylation at the C-2 position of hopanoids increases rigidity in native bacterial membranes. *eLife*, 4, e05663.

Yin, L. & Yuan, X. (2007) Radiation of Meso–Neoproterozoic and early Cambrian protists inferred from the microfossil record of

China. *Palaeogeography, Palaeoclimatology, Palaeoecology*, 254, 350–361.

Zanatta, A.R. & Ferri, F. (2007) Crystallization, stress and stress-relieve due to nickel in amorphous silicon thin films. *Journal of Applied Physics*, 102, 043509.

SUPPORTING INFORMATION

Additional supporting information can be found online in the Supporting Information section at the end of this article.

How to cite this article: Álvaro, J.J., Ortiz, J.E., Neto de Carvalho, C., López-Cilla, I., Sánchez-Palencia, Y. & Torres, T. (2023) Biogenicity of amorphous organic matter and bacteriomorph acritarchs preserved in wrinkle structures from the Ediacaran Cíjara Formation, Spain. *The Depositional Record*, 00, 1–19. Available from: https://doi.org/10.1002/dep2.258